

# VIRCHOW: A MILLION-SLIDE DIGITAL PATHOLOGY FOUNDATION MODEL

A PREPRINT

Eugene Vorontsov<sup>†1</sup>, Alican Bozkurt<sup>†1</sup>, Adam Casson<sup>†1</sup>, George Shaikovski<sup>†1</sup>, Michal Zelechowski<sup>†1</sup>, Siqi Liu<sup>†\*</sup>, Philippe Mathieu<sup>1</sup>, Alexander van Eck<sup>1</sup>, Donghun Lee<sup>1</sup>, Julian Viret<sup>1</sup>, Eric Robert<sup>1</sup>, Yi Kan Wang<sup>1</sup>, Jeremy D. Kunz<sup>1</sup>, Matthew C. H. Lee<sup>1</sup>, Jan H. Bernhard<sup>1</sup>, Ran A. Godrich<sup>1</sup>, Gerard Oakley<sup>1</sup>, Ewan Millar<sup>2</sup>, Matthew Hanna<sup>1,3</sup>, Juan Retamero<sup>1</sup>, William A. Moya<sup>1</sup>, Razik Yousfi<sup>1</sup>, Christopher Kanan<sup>1,4</sup>, David Klimstra<sup>1,3</sup>, Brandon Rothrock<sup>1</sup>, and Thomas J. Fuchs<sup>1</sup>

<sup>1</sup>Paige, NYC, NY United States

<sup>2</sup>NSW Health Pathology, St George Hospital, Sydney Australia

<sup>3</sup>Memorial Sloan Kettering Cancer Center, NYC, NY United States

<sup>4</sup>University of Rochester, Rochester, NY United States

## ABSTRACT

Computational pathology uses artificial intelligence to enable precision medicine and decision support systems through the analysis of whole slide images. It has the potential to revolutionize the diagnosis and treatment of cancer. However, a major challenge to this objective is that for many specific computational pathology tasks the amount of data is inadequate for development. To address this challenge, we created Virchow, a 632 million parameter deep neural network foundation model for computational pathology. Using self-supervised learning, Virchow is trained on 1.5 million hematoxylin and eosin stained whole slide images from diverse tissue groups, which is orders of magnitude more data than previous works. When evaluated on downstream tasks including tile-level pan-cancer detection and subtyping and slide-level biomarker prediction, Virchow outperforms state-of-the-art systems both on internal datasets drawn from the same population as the pretraining data as well as external public datasets. Virchow achieves 93% balanced accuracy for pancancer tile classification, and AUCs of 0.983 for colon microsatellite instability status prediction, 0.910 for bladder FGFR status prediction, and 0.841 for lung EGFR status prediction. The gains in performance highlight the importance of pretraining on massive pathology image datasets, suggesting pretraining on even larger datasets could continue improving performance for many high-impact applications where limited amounts of training data are available, such as drug outcome prediction.

## 1 Introduction

Pathology impacts nearly every aspect of medicine, and it is essential for the diagnosis and treatment of cancer. Computational pathology uses artificial intelligence applied to digitized whole slide images (WSIs) of glass slides in order to provide advanced analytics to support diagnosis and the understanding of disease. Recent advancements in computational pathology have shown great promise for enhancing personalized medicine through the detection of biomarkers using routine samples instead of specialized and often expensive reflex testing. It is also being used to help pathologists diagnose cancer faster and more accurately [da Silva et al., 2021, Perincheri et al., 2021, Raciti et al., 2020, Campanella et al., 2019]. The use of computational pathology to predict biomarkers from the canonical hematoxylin and eosin (H&E) stained microscopy slides could greatly reduce medical costs by reducing the need for

\*Corresponding Author. Email: siqi.liu AT paige DOT ai

<sup>†</sup>These authors contributed equally to this work.

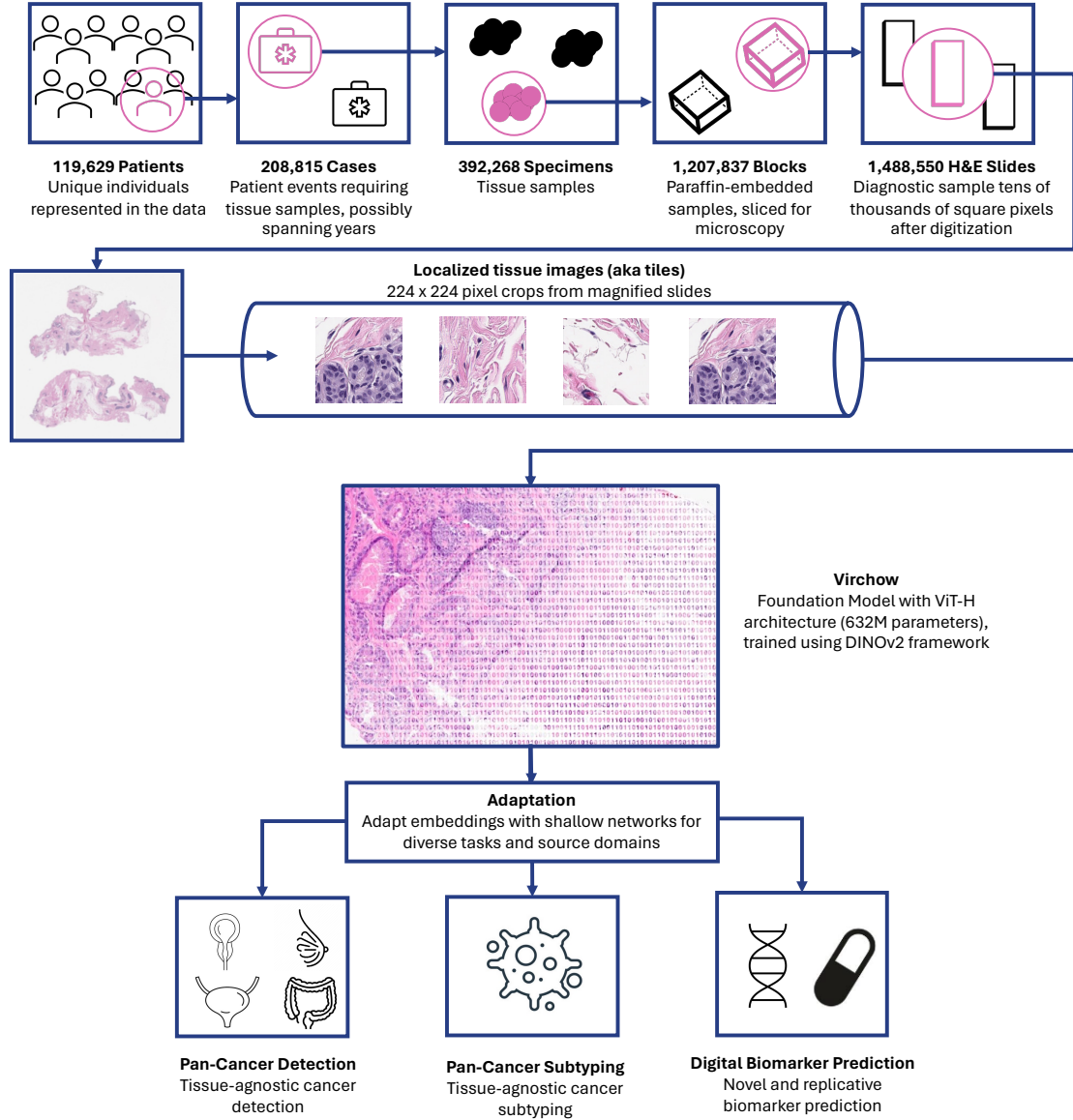


Figure 1: Virchow model dataflow and applications. The Virchow model is a digital pathology foundation model trained on 1.5 million WSIs of various tissues and cancers. It takes slide tiles as inputs and outputs embeddings for downstream pathology applications such as pan-cancer detection, cancer subtyping, and biomarker prediction.

immunohistochemistry (IHC) or genomic testing and enable oncologists to receive diagnostic information critical for effective treatment planning more rapidly.

Until recently, computational pathology systems have been created using large amounts of labeled data, either by having pathologists annotate pixels in WSIs, or by training with weak supervision on thousands of WSIs from a specific tissue type [Casson et al., 2023, Campanella et al., 2019]. This strategy cannot be employed for rare cancers or biomarkers, where there is an insufficient amount of data. A new paradigm has emerged in artificial intelligence based on very large deep neural networks trained on enormous datasets, termed *foundation models*. Foundation models employ self-supervised learning and exhibit emergent properties that facilitate high performance on a diversity of downstream tasks [Bommasani et al., 2021].

Here, we present the world’s largest foundation model for pathology, named *Virchow* in honor of Rudolf Virchow (pronounced vir-kov), the father of modern pathology [Schultz, 2008, Reese, 1998], who proposed the first theory of cellular pathology [Virchow, 1860]. As shown in Figure 1, Virchow is trained on 1.5 million WSIs and includes a diverse sampling of tissue types, which is orders of magnitude larger than prior self-supervised systems in pathology. We evaluate Virchow on tile-level pan-cancer detection and subtyping and slide-level biomarker prediction, both on internal datasets drawn from the same population as the pretraining data and on external public datasets.

This working draft presents our initial results that will be revised over time as experiments continue to scale.

## 2 Data and Methods

### 2.1 Million-scale pre-training dataset

For the self-supervised pre-training of Virchow, we amassed a digital pathology dataset on an unprecedented scale. This dataset, sourced from the Memorial Sloan Kettering (MSK) Cancer Center comprises 1,488,550 WSIs derived from 119,629 patients. These WSIs are a mix of 20 $\times$  and 40 $\times$  scans, all of which are stained with H&E which is considered the gold standard in pathology, resulting in the nuclei being stained blue while the extracellular matrix and cytoplasm are stained pink.

We assembled the pretraining dataset to ensure it encompassed 24 distinct tissue types of significant relevance to the field of digital pathology AI applications. These tissue types further belong to 17 high-level tissue groups, as illustrated in Figure 2.

To estimate the clinical cancer or cancer-precursor diagnosis at the specimen level, a rule-based natural language processing system was employed. This system decomposes case-level reports to the specimen level and analyzes the associated clinical reports with each specimen, thereby providing a comprehensive understanding of each case. According to the analysis, out of 392,268 specimens in total, 129,469 specimens contain cancer and 64,451 specimens contain cancer precursors.

During distributed training, we select one slide per GPU from the dataset, then select 256 tiles from each slide, and use these tiles to form local mini-batches. Once we have processed the given set of tiles, we select a new slide for each GPU and repeat the process.

### 2.2 Leveraging ViT-Huge and DINOv2 for Histopathology Image Analysis

Virchow employs the vision transformer (ViT)-Huge architecture (ViT-H/14), a vision transformer [Dosovitskiy et al., 2020] with 632 million parameters, and is trained using the DINOv2 [Oquab et al., 2023] self-supervised learning algorithm as illustrated in Figure A2. DINOv2 has recently achieved state of the art performance on many general vision tasks, and is based on a student-teacher paradigm. Given a student network and a teacher network, the student seeks to match the representation of the teacher. The student network is information-limited, as it is trained using random crops of an input image. The teacher network is a slowly updated exponential moving average of past student networks; matching the teacher achieves an effect similar to that of ensembling over prior student predictions [Tavainen and Valpola, 2017]. The student learns a representation on a global image level by matching the teacher’s class token, as well as on a local patch level by matching the teacher’s token representation for tokens masked out in the image, as in masked image modeling [Xie et al., 2022]. Additional regularization helps DINOv2 trained models outperform the earlier DINO variant.

The choice of a mean teacher based method like DINOv2 is more suitable for histopathology images than earlier contrastive methods (e.g., CTransPath [Wang et al., 2022]) because the linear separability of the representation produced by contrastive methods suffers when data is class-imbalanced [Assran et al., 2022]. Training on histopathology data poses a few unique challenges in dealing with class imbalance. Pathological features are anomalous and thus rare,

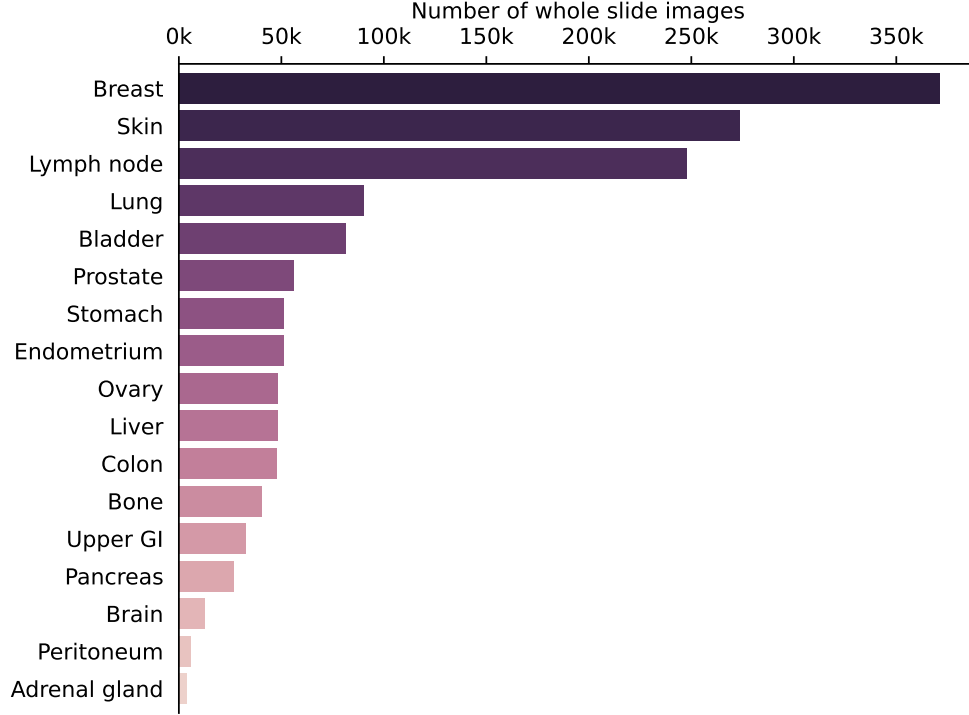


Figure 2: The number of pretraining WSIs stratified by the high-level tissue groups.

and rare pathologies are ideally detectable with high sensitivity. Although both mean teacher based methods like DINOv2 and reconstruction based methods such as the masked autoencoder (MAE) [He et al., 2022] perform well on class-imbalanced data, the representations produced by the latter yield worse linear probing performance without an additional finetuning step [He et al., 2022, Shekhar et al., 2023].

We used the default hyperparameters for pre-training the DINOv2 model, as detailed in Oquab et al. [2023] with the following changes: a learning rate warmup of 495,000 iterations (instead of 100,000) and a teacher temperature schedule of 0.04 to 0.07 in 186,000 iterations. We trained using AdamW ( $\beta_1 = 0.9$ ,  $\beta_2 = 0.999$ ) with float16 precision. Note that with ViT-H, we used 131,072 prototypes (and thus 131,072-dimensional projection heads). For a  $224 \times 224$  input tile image, we define an embedding as the concatenation of the class token and the mean across all 256 of the other predicted tokens. This produces an embedding size of 2,560 ( $1,280 \times 2$ ).

### 3 Results

Virchow produces rich tile embeddings which can be used in a variety of downstream tasks, including class prediction on individual tiles, and slide-level aggregation to enable prediction on WSIs or collections of WSIs from a patient. We investigated the quality of Virchow’s representations using both internally developed and publicly available downstream tasks, such as cancer detection and subtyping at the tile level, and biomarker prediction at the slide level.

#### 3.1 Tile-level benchmarks

We performed linear probing on labeled tiles from pathology slides both from internally collected data and from public datasets. The internal multi-tissue dataset for pancancer detection at the tile level (PanMSK) can be seen as an in-distribution (ID) benchmark, as it is composed from annotations on a held-out set of slides across all the tissue groups of the Virchow’s MSK pre-training dataset. On the other hand, the public datasets can be seen as out-of-distribution (OOD) benchmarks. These include multi-class colorectal cancer classification (NCT-CRC-HE-100K and NCT-CRC-HE-100K-NONORM, [Kather et al., 2018, 2019]), colorectal polyp classification (MHIST, [Wei et al., 2021]), and breast lymph node cancer classification (PatchCamelyon (PCam), [Veeling et al., 2018, Bejnordi et al., 2017])). Dataset details are listed in Table 1.



Dataset	Tissue	High-Level Tissue Types	Classes	Res	Tile size	No. of tiles
PanMSK	PanCancer	17	2	20×	224×224	1,196,171
CRC	Colon	1	9	20×	224×224	107,180
MHIST	Colon	1	2	40×	224×224	3,152
PCam	Lymph node	1	2	10×	96×96	327,680

Table 1: Summary of the tile-level benchmark datasets used for linear probing.

For each experiment, we trained a linear tile classifier with a batch size of 4,096 using the stochastic gradient descent (SGD) optimizer with a cosine learning rate schedule, from 0.001 to 0 (0.01 to 0 for MHIST), for 200 epochs (CRC), 3,000 epochs (MHIST), 300 epochs (PCam), or 30 epochs (PanMSK), on top of the frozen Virchow encoder, CTransPath encoder, or Owkin PanCancer encoder. Linear probing experiments did not use data augmentation.

**Metrics.** We report accuracy, balanced accuracy, and weighted F1 score in Table 2. Balanced accuracy is calculated by averaging true positive rate (TPR) ( $\text{TPR} = \frac{\text{TP}}{\text{TP} + \text{FN}}$ ) and true negative rate (TNR) ( $\text{TNR} = \frac{\text{TN}}{\text{TN} + \text{FP}}$ ). Weighted F1 score is calculated by first calculating the F1 score (harmonic mean of precision and recall) for each class and then averaging the scores, weighted by the number of positive samples for each class. For balanced accuracy and weighted F1 score calculation, we use the probability threshold = 0.5 as the operating point.

Dataset	Metric	DINO <sub>p=8</sub>	UNI	Owkin	CTransPath	Virchow
PanMSK	Accuracy	-	-	0.900	0.851	<b>0.928</b>
	Balanced Accuracy	-	-	0.900	0.851	<b>0.928</b>
	Weighted F1	-	-	0.899	0.846	<b>0.928</b>
CRC	Accuracy	0.953	-	0.946	0.958	<b>0.968</b>
	Balanced Accuracy	-	-	0.937	0.931	<b>0.956</b>
	Weighted F1	-	-	0.948	0.955	<b>0.968</b>
CRC (no norm)	Accuracy	-	-	0.895	0.879	<b>0.948</b>
	Balanced Accuracy	-	0.874	0.887	0.852	<b>0.938</b>
	Weighted F1	-	0.875	0.902	0.883	<b>0.950</b>
MHIST	Accuracy	0.779	-	0.793	0.789	<b>0.827</b>
	Balanced Accuracy	-	-	0.774	0.747	<b>0.809</b>
	Weighted F1	-	-	0.780	0.780	<b>0.828</b>
PCam	Accuracy	0.901	-	0.909	0.858	<b>0.927</b>
	Balanced Accuracy	-	-	0.909	0.858	<b>0.926</b>
	Weighted F1	-	-	0.909	0.858	<b>0.926</b>

Table 2: Downstream task linear probing evaluations. Refer to the text for details on the metrics. Values for DINO<sub>p=8</sub> and UNI are taken from [Kang et al., 2023] and [Chen et al., 2023] respectively.

**PanMSK.** For a comprehensive ID benchmark, 3,999 slides were held-out from the pre-training dataset collected from MSK. Of these, 1,456 contained cancer that was either partially or exhaustively annotated with segmentation masks by board-certified pathologists. These annotations were used to create a tile-level dataset of cancer vs non-cancer classification which we refer to as *PanMSK*. All images in PanMSK are 224×224 pixel tiles at 0.5 microns-per-pixel (mpp).

Exhaustive annotations (i.e. a complete segmentation of cancer vs non-cancer regions across the entire WSI) were collected for 399 prostate slides, 187 breast slides, 115 bladder slides, 64 breast lymph node slides, and 55 colon slides by a different pathologist for each tissue group. For the other tissue groups (see Figure 2), a pathologist highlighted one or more cancer regions on each slide non-exhaustively. The fully-annotated 64 breast lymph node slides were combined with 48 lymph node slides with highlighted cancer regions, originating from various locations. We sampled non-cancer tiles from slides labeled as benign. With the exception of the endometrial tissue group (for which we selected cancer regions in 11 slides), no tissue group had less than 50 slides partially or thoroughly annotated. We found that when randomly splitting the data into training, validation, and testing subsets, we need at least 30 slides per tissue

group to minimize the chance that the training set is not a representative sample of the test set; therefore, we preferred maximizing slide and patient diversity over maximizing how much of each slide is annotated.

PanMSK was split into training, validation, and testing subsets at the slide level, ensuring that no two subsets share tiles from the same slide. The subsets were balanced to achieve an approximately 7:1:2 ratio of both slides *and* tiles, to equalize the ratio of tile diversity to tile quantity across all splits. The slides were divided into training, validation, and testing subsets by the tissue group and slide-level label (cancer/benign). In order to reduce tissue bias, the number of available cancer tiles for the tissue groups with the most cancer tiles was reduced to the median number of cancer tiles across all tissue groups. The optimal training/validation/testing split was then determined algorithmically by matching the distribution over tissue groups and over labels as closely as possible across all splits. This objective was optimized iteratively. In each iteration, slides were randomly shuffled between the splits and a permutation was picked greedily to maximize the objective. After balancing cancer tiles across the training, validation, and testing subsets and across tissue groups, benign tiles were sampled per tissue group to achieve a 1:1 ratio between cancer and benign tiles. See Figure A1 and Table 3 for more information on PanMSK splits.

As shown in Table 2, Virchow strongly outperforms CTransPath on PanMSK in accuracy (0.928 vs 0.851) and F1 score (0.928 vs 0.846) with linear probing. For PanMSK, accuracy is equivalent to balanced accuracy since the classes are balanced.

Split	Slides	Cancer tiles	Benign tiles
Training	2,797	418,738	417,466
Validation	402	60,462	60,296
Testing	800	119,792	119,417

Table 3: Slide and tile counts in PanMSK. The tiles were split into train, validation, and test subsets with no slide overlap between the subsets. They follow a 7:1:2 split on both the slide- and tile-level.

**CRC.** The colorectal cancer (CRC) classification public dataset [Kather et al., 2019] contains 100,000 images ( $224 \times 224$  pixels) at  $20\times$  magnification sorted into nine morphological classes. We performed linear probing with both the Macenko-stain-normalized (NCT-CRC-HE-100K) and unnormalized (NCT-CRC-HE-100K-NONORM) variants of the dataset. In both cases, Virchow outperformed baseline methods (Table 2). All models performed well on the stain-normalized version of CRC (“CRC” in Table 2): Virchow and CTransPath reached 0.968 and 0.958 accuracy respectively, whereas a prior DINO model is reported to reach 0.953 [Kang et al., 2023]. When using the more challenging and realistic unnormalized version (“CRC (no norm)” in Table 2), Virchow greatly improved over baseline methods with a balanced accuracy of 0.938, compared to 0.874 with UNI [Chen et al., 2023] and 0.852 with CTransPath.

**MHIST.** The colorectal polyp classification public dataset (MHIST, [Wei et al., 2021]) contains 3,152 images ( $224 \times 224$  pixels) presenting either hyperplastic polyp or sessile serrated adenoma at  $5\times$  magnification (downsampled from  $40\times$  to increase the field of view). As shown in Table 2, linear probing with Virchow clearly outperformed the baseline methods on MHIST by all metrics. While Virchow reached 0.827 accuracy, CTransPath reached 0.789 accuracy, followed by the DINO model of Kang et al. [2023] which reached 0.779.

**PCam.** The PCam public dataset consists of 327,680 images ( $96 \times 96$  pixels) at  $10\times$  magnification, downsampled from  $40\times$  to increase the field of view [Veeling et al., 2018, Bejnordi et al., 2017]. Images are labeled as either cancer or benign. We upsampled the images to  $224 \times 224$  pixels to use with Virchow. With linear probing experiments (Table 2), Virchow achieved 0.927 accuracy, greatly outperforming CTransPath (0.858 accuracy) and the DINO-trained model by Kang et al. [2023] (0.901 accuracy).

### 3.2 Slide-level benchmarks

We aimed to evaluate the performance of Virchow at the whole slide level using several high-impact biomarkers that can be predicted from H&E staining. These biomarkers are Colon Microsatellite Instability (MSI), Bladder Fibroblast Growth Factor Receptor (FGFR), and Lung Epidermal Growth Factor Receptor (EGFR). These biomarkers play a crucial role in the diagnosis and treatment of various cancers.

We use the area under the receiver operating characteristic (AUROC) to measure the performance. AUROC is calculated by plotting TPR against false positive rate (FPR) ( $FPR = \frac{FP}{FP+TN}$ ) for all operating points and calculating the area under the curve.

Split	ColonMSI			BladderFGFR			LungEGFR		
	Cases	Slides	Positive ratio	Cases	Slides	Positive ratio	Cases	Slides	Positive ratio
Training	2,029	2,291	0.10	520	542	0.24	2,216	2,960	0.28
Validation	334	384	0.12	259	275	0.29	367	488	0.27
Testing	335	373	0.13	259	270	0.25	359	466	0.28

Table 4: Statistics of the case-level biomarker target datasets, including the number of cases, the number of slides, and the proportion of positive labels.

Backbone	AUROC		
	ColonMSI	BladderFGFR	LungEGFR
CTransPath	0.971	0.897	0.783
Virchow	<b>0.983</b>	<b>0.910</b>	<b>0.841</b>

Table 5: Case-level AUROC scores on the test set for different biomarker targets using the aggregator network trained on tile-level embeddings from the CTransPath model and our Virchow model.

### 3.2.1 Evaluation Datasets

Samples included in the evaluation datasets had been previously subjected to targeted sequencing using the FDA-authorized MSK-Integrated Mutation Profiling of Actionable Targets (MSK-IMPACT) assay. WSIs from the histologic sections matching the respective blocks utilized for DNA extraction and MSK-IMPACT sequencing [Zehir et al., 2017] were utilized. MSK-IMPACT targeted sequencing data was analyzed to determine the status of genetic alterations and establish a binary label indicating the presence or absence of the variants, i.e. the biomarker.

We formulated each biomarker prediction as a binary pathology case classification problem, where a positive label indicates the presence of the biomarker. Each case consists of one or more H&E slides that share the same binary label. We randomly split each dataset into training, validation, and testing subsets, ensuring no patient overlap, as shown in Table 4.

**MSI** describes a state in which regions of DNA with short repeating sequences called microsatellites are interrupted by single nucleotide mutations in the repeating sequence, creating inconsistent blocks of the repeated sequence between cells [CDC, 2023]. Ordinarily, these single nucleotide changes are repaired by the cell due to the action of the mismatch repair (MMR) genes MSH1, MSH2, MSH6, and PMS2, keeping the repeating sequences intact and thus the same number of repeating sequences of DNA in microsatellites the same between cells. Inactivation of one of these genes, either by germline mutation, somatic mutation, or epigenetic silencing, increases the rate at which single nucleotide mutations are not effectively repaired across the genome. Assay of microsatellites by PCR or next generation sequencing (NGS) based methods can detect increased numbers of unrepaired single nucleotide mutations in microsatellites, thus providing a biomarker for the functional status of the MMR genes. A high frequency of sequence repeat inconsistencies in microsatellites is called MSI-H, and indicates a deficient mismatch repair (dMMR) mechanism in the affected cells. dMMR can also be tested by IHC, where mutation or epigenetic silencing will frequently absent staining for the four MMR proteins, with the pattern of absence indicating the gene most likely silenced. Carcinomas with a dMMR or MSI-H diagnosis may qualify for treatment with checkpoint inhibitors. MSI-H is found in about 15% of all CRC [Gatalica et al., 2016], and a significant portion of these have a germline mutation indicating increased hereditary cancer risk in close family members if they carry the same mutation. Hence, it is regarded as best practice to screen every primary sample of colorectal carcinoma for molecular MSI or IHC-based dMMR [Gupta et al., 2019]. For our ColonMSI dataset, we composed a ground truth label that considers IHC and MSK-IMPACT sequencing test results for dMMR and MSI-H, respectively. If test results from both methods are available, the resulting binary label gives preference to the IHC-based test result. The ColonMSI dataset composes a total of 2,698 CRC samples of which 288 samples are positive for dMMR/MSI-H.

**FGFR alterations** screening in bladder carcinoma allows the identification of patients targetable by FGFR inhibitors. Anecdotal experience from pathologists suggested there may be a morphologic signal for FGFR alterations [Al-Ahmadie et al., 2011]. The FGFR3 binary label focuses on FGFR3 p.S249C, p.R248C, p.Y373C mutations and FGFR3-TACC3 fusions based on data from the MSK-IMPACT cohort. From the total of 1051 WSIs, 25.8% have FGFR3 alterations.

**EGFR oncogenic mutation** screening in non-small cell lung cancer (NSCLC) is essential to determine eligibility for targeted therapies in late stage NSCLC [Kalemkerian et al., 2018]. The oncogenic status of EGFR mutation was determined based on OncoKB annotation [Chakravarty et al., 2017]. EGFR mutations with any oncogenic effect (including predicted/likely oncogenic) were defined as positive label, and EGFR mutation with unknown oncogenic status were excluded. 2,942 NSCLC samples were included for the EGFR dataset, of which 828 were positive samples.

### 3.2.2 Experiment Setup

For weakly supervised biomarker prediction, we used Agata [Raciti et al., 2022], a weakly supervised multiple instance learning aggregator network, to transform a set of tiles extracted from WSIs belonging to the same case to case-level target labels. This aggregator network learns to attend to tiles that contribute toward the case-level label.

Given query  $Q$ , key  $K$ , and value matrix  $V$ , the cross attention is formulated as  $\text{softmax}(QK^T/\sqrt{d_k})V$ , where  $d_k$  is the output dimension of the key matrix. In contrast to the typical cross attention mechanism where  $Q, K, V$  are projected from the inputs,  $Q$  is parameterized directly by the model to reduce GPU memory consumption.  $K$  and  $V$  are obtained with two consecutive Gaussian Error Linear Unit (GELU) [Hendrycks and Gimpel, 2016] projection layers as:

$$\begin{aligned} K &= \text{GELU}(W_1^T x + b_1), \\ V &= \text{GELU}(W_2^T K + b_2), \end{aligned} \tag{1}$$

where  $x$  is the tile embedding. In our experiments,  $W_1$  produces 256-dimensional keys,  $W_2$  produces 512-dimensional values, and we omit scaling by  $\sqrt{d_k} = 16$ .

Virchow is used to generate tile level embeddings on all the evaluated datasets with  $224 \times 224$  resolution at  $20 \times$  magnification. The aggregator networks were trained on the training sets. We selected the best aggregator model based on the AUROC score on the validation sets. We used the publicly available CTransPath model [Wang et al., 2022] as a baseline for comparison. Due to the differences between datasets and compared models, we performed a grid search for the initial learning rate of the aggregator training among  $1 \times 10^{-3}$ ,  $1 \times 10^{-4}$  and  $3 \times 10^{-5}$  and report the best observed test AUROC scores in Table 5. The results indicate that the Virchow model outperforms the baseline model on all four biomarker targets.

### 3.3 Semantic features

In order to qualitatively evaluate whether the low level features learnt by Virchow tend to separate the image into semantically meaningful clusters, we performed an unsupervised feature analysis similar to the procedure in Oquab et al. [2023]. We visualized this feature separation on the CoNSeP dataset [Graham et al., 2019] of H&E stained slides with colorectal adenocarcinoma. CoNSeP provides nuclear annotations of cells in the following 7 categories: normal epithelial, malignant/dysplastic epithelial, fibroblast, muscle, inflammatory, endothelial, and miscellaneous (including necrotic, mitotic, and cells that couldn't be categorized). Since CoNSeP images are of size  $1,000 \times 1,000$  and Virchow takes in images of size  $224 \times 224$ , we resized images to  $896 \times 896$  and divided them into a  $4 \times 4$  grid of non-overlapping  $224 \times 224$  sub-images before extracting patch-level features. For a given image, we used principal component analysis (PCA) on all the patch features from the sub-images, normalized the first and second principal components to values within  $[0, 1]$ , and thresholded at 0.5. Figure 3 shows some examples of the unsupervised feature separation achieved in this way.

Interestingly, we observe approximate semantic segmentation of the cell types in the CoNSeP images. For the first three examples in Figure 3 (top to bottom), malignant epithelium (● red) was highlighted by the first principal component. In the fourth and fifth examples, the first principal component is not as granular; however, normal epithelium (● green) and muscle (● cyan) were highlighted by the second principal component. The latter is a particularly interesting example since the structures are so small, elongated, and isolated. In the last example (bottom row), malignant epithelium (● red) is captured by the second principal component. DINOv2 has been shown to learn a similar semantic feature separation on natural images, allowing foreground/background separation (e.g. discriminating a bus or a bird from the background) as well as part annotation (e.g. wheels vs windows in a bus) [Oquab et al., 2023]. Here, we show that this emerging property of the model carries over to the pathology domain. This encouraging result supports our expectation that the unsupervised features learnt by Virchow are meaningful and interpretable for a wide range of downstream tasks, from annotation at the cellular level up through prediction and diagnosis at the slide level.



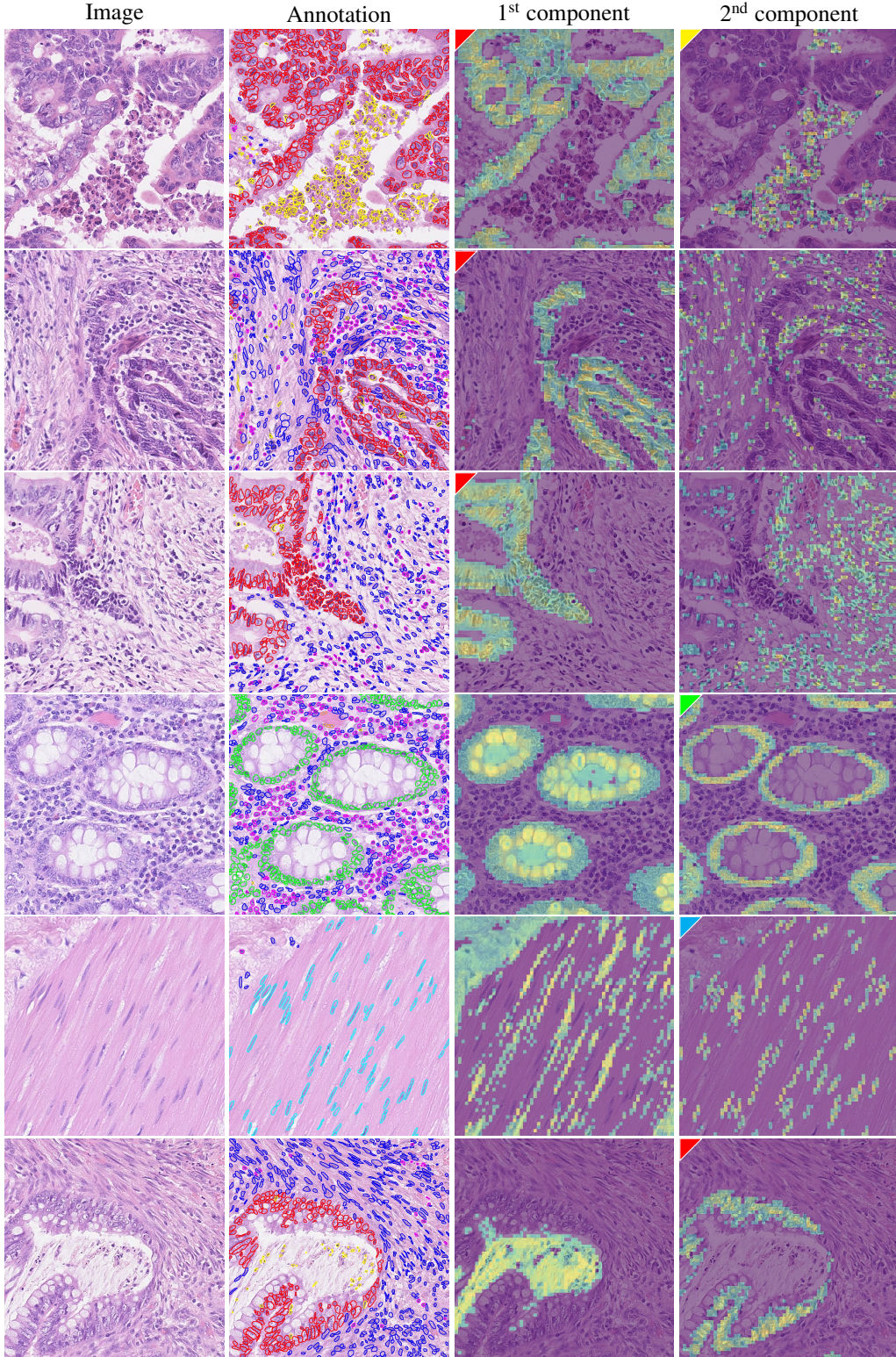


Figure 3: Using PCA, we visualized the representations learnt by Virchow using the colorectal nuclear segmentation and phenotypes (CoNSeP) dataset [Graham et al., 2019]. As an emergent property of its self-supervised training, it discovers clinically relevant morphological features. For the 1<sup>st</sup> or 2<sup>nd</sup> components, the triangle color in the top left corner corresponds to the color of the best matching annotation: malignant epithelium (● red), miscellaneous (● yellow), normal epithelium (● green), and muscle (● cyan).

## 4 Related Work

A variety of self-supervised systems for computational pathology have been created in the past few years. Chen et al. [2022] introduced the Hierarchical Image Pyramid Transformer (HIPT), a ViT with less than 10 million parameters trained on approximately 100 million patches extracted from 11 thousand WSIs from The Cancer Genome Atlas (TCGA) Weinstein et al. [2013]. HIPT was trained with student-teacher knowledge distillation (DINO [Caron et al., 2021]) at two successive levels of representation: local image patches, followed by regional image patches derived from the learnt representations of multiple local patches. Wang et al. [2022] proposed CTransPath, a Swin transformer (with a convolutional backbone) with 28 million parameters, trained on 15 million patches extracted from 30 thousand WSIs (TCGA and PAIP [Kim et al., 2021]). CTransPath improved over MoCo v3 [Chen et al., 2021] by using the memory bank to mine pseudo-positive examples for the contrastive loss [Chen et al., 2020]. Similarly, Ciga et al. [2022] trained a 45 million parameter ResNet on 25 thousand WSIs with the addition of 39 thousand patches, all collected from TCGA and 56 other small datasets. Recently, Filiot et al. [2023] trained a ViT-Base architecture with 86 million parameters using the image BERT pre-training with Online Tokenizer (iBOT) framework [Zhou et al., 2021]. This model was pretrained on 43 million patches extracted from 6 thousand WSIs (TCGA) and outperformed HIPT and CTransPath on a variety of TCGA evaluation tasks. It followed up on earlier smaller scale work [Dehaene et al., 2020]. Similarly, Azizi et al. [2023] trained a 60 million parameter model with SimCLR [Chen et al., 2020] on 29 thousand WSIs, comprising nearly the entire TCGA dataset.

These studies use models with at most 86 million parameters. They employ a mean teacher distillation objective for training on TCGA data, which comprises over 30 thousand WSIs. In contrast, Virchow stands out with its significantly larger scale and extensive training data. It has 632 million parameters, which is a 69-fold increase in size compared to the largest models used in the aforementioned studies. Furthermore, Virchow is trained on tile images extracted from 1.5 million WSIs – a volume of data that is over three thousand times the number of pixels found in ImageNet [Deng et al., 2009]. Current foundation models in language and image domains are built on large datasets with billions of examples, learnt by high capacity models with billions of parameters [Dehghani et al., 2023, Driess et al., 2023, Alayrac et al., 2022]. It has been observed that very large parameter and dataset scales are necessary to achieve a *phase transition* toward emergent properties in foundation models [Wei et al., 2022]. We therefore hypothesize that the quantity and variety of data, along with a sufficiently large model to fit the data, are more important factors in developing a foundation model than specific architectural choices. This is supported by prior work that found there was no clear winner when training four different self-supervised algorithms on 37 thousand WSIs [Kang et al., 2023]. Nevertheless, Virchow is trained with DINOv2 due to its state of the art effectiveness and computational efficiency [Oquab et al., 2023], which was also used in concurrent work where a model was trained on 100 thousand WSIs [Chen et al., 2023].

## 5 Conclusion

In this paper, we demonstrate that self-supervised learning at scale on histopathology data yields the best-performing pathology foundation model to date, Virchow. We will continue to work on scaling the model and dataset sizes. We plan to also extend the analysis in this work to include few-shot performance. Furthermore, we plan to better interrogate Virchow’s performance by investigating unwanted data memorization (as done by Guo et al. [2023]), exploring the effect of pre-training data balancing by tissue group, and preparing a more challenging benchmark dataset to evaluate performance on uncommon cancers.

## Acknowledgements

We would like to express our profound gratitude to Kristen Severson, Jimmy Hall, Neil Tenenholtz, Nicolo Fusi, and Philip Rosenfield from Microsoft Research for their invaluable advice and insightful feedback on our past and ongoing collaboration. Their exceptional expertise has been instrumental in significantly shaping the trajectory of our work and the overall quality of this manuscript.

## References

Hikmat A Al-Ahmadie, Gopa Iyer, Manickam Janakiraman, Oscar Lin, Adriana Heguy, Satish K. Tickoo, Samson W. Fine, Anuradha Gopalan, Ying-bei Chen, Arjun Balar, Jamie Riches, Bernard Bochner, Guido Dalbagni, Dean F. Bajorin, Victor E. Reuter, Matthew I. Milowsky, and David B. Solit. Somatic mutation of fibroblast growth factor receptor-3 (FGFR3) defines a distinct morphological subtype of high-grade urothelial carcinoma. *The Journal of*

- Pathology*, 224(2):270–279, June 2011. ISSN 00223417. doi:10.1002/path.2892. URL <http://doi.wiley.com/10.1002/path.2892>.
- Jean-Baptiste Alayrac, Jeff Donahue, Pauline Luc, Antoine Miech, Iain Barr, Yana Hasson, Karel Lenc, Arthur Mensch, Katherine Millican, Malcolm Reynolds, et al. Flamingo: a visual language model for few-shot learning. *Advances in Neural Information Processing Systems*, 35:23716–23736, 2022.
- Mahmoud Assran, Randall Balestrieri, Quentin Duval, Florian Bordes, Ishan Misra, Piotr Bojanowski, Pascal Vincent, Michael Rabbat, and Nicolas Ballas. The hidden uniform cluster prior in self-supervised learning. *arXiv preprint arXiv:2210.07277*, 2022.
- Shekoofeh Azizi, Laura Culp, Jan Freyberg, Basil Mustafa, Sebastien Baur, Simon Kornblith, Ting Chen, Nenad Tomasev, Jovana Mitrović, Patricia Strachan, et al. Robust and data-efficient generalization of self-supervised machine learning for diagnostic imaging. *Nature Biomedical Engineering*, pages 1–24, 2023.
- Babak Ehteshami Bejnordi, Mitko Veta, Paul Johannes Van Diest, Bram Van Ginneken, Nico Karssemeijer, Geert Litjens, Jeroen AWM Van Der Laak, Meyke Hermesen, Quirine F Manson, Maschenka Balkenhol, et al. Diagnostic assessment of deep learning algorithms for detection of lymph node metastases in women with breast cancer. *Jama*, 318(22):2199–2210, 2017.
- Geert Berx and Frans Van Roy. The e-cadherin/catenin complex: an important gatekeeper in breast cancer tumorigenesis and malignant progression. *Breast Cancer Research*, 3:289–293, 2001. doi:10.1186/bcr309.
- Rishi Bommasani, Drew A Hudson, Ehsan Adeli, Russ Altman, Simran Arora, Sydney von Arx, Michael S Bernstein, Jeannette Bohg, Antoine Bosselut, Emma Brunskill, et al. On the opportunities and risks of foundation models. *arXiv preprint arXiv:2108.07258*, 2021.
- Gabriele Campanella, Matthew G Hanna, Luke Geneslaw, Allen Miraflor, Vitor Werneck Krauss Silva, Klaus J Busam, Edi Brogi, Victor E Reuter, David S Klimstra, and Thomas J Fuchs. Clinical-grade computational pathology using weakly supervised deep learning on whole slide images. *Nature medicine*, 25(8):1301–1309, 2019.
- Mathilde Caron, Hugo Touvron, Ishan Misra, Hervé Jégou, Julien Mairal, Piotr Bojanowski, and Armand Joulin. Emerging properties in self-supervised vision transformers. In *Proceedings of the IEEE/CVF international conference on computer vision*, pages 9650–9660, 2021.
- Adam Casson, Siqi Liu, Ran A Godrich, Hamed Aghdam, Donghun Lee, Kasper Malfroid, Brandon Rothrock, Christopher Kanan, Juan Retamero, Matt Hanna, et al. Joint breast neoplasm detection and subtyping using multi-resolution network trained on large-scale h&e whole slide images with weak labels. In *Medical Imaging with Deep Learning*, 2023.
- CDC. Microsatellite Instability (MSI) screening | CDC, June 2023. URL [https://www.cdc.gov/genomics/disease/colorectal\\_cancer/MSI.htm](https://www.cdc.gov/genomics/disease/colorectal_cancer/MSI.htm).
- Debyani Chakravarty, Jianjiong Gao, Sarah Phillips, Ritika Kundra, Hongxin Zhang, Jiaojiao Wang, Julia E Rudolph, Rona Yaeger, Tara Soumerai, Moriah H Nissan, et al. Oncokb: a precision oncology knowledge base. *JCO precision oncology*, 1:1–16, 2017.
- Richard J Chen, Chengkuan Chen, Yicong Li, Tiffany Y Chen, Andrew D Trister, Rahul G Krishnan, and Faisal Mahmood. Scaling vision transformers to gigapixel images via hierarchical self-supervised learning. In *Proceedings of the IEEE/CVF Conference on Computer Vision and Pattern Recognition*, pages 16144–16155, 2022.
- Richard J. Chen, Tong Ding, Ming Y. Lu, Drew F. K. Williamson, Guillaume Jaume, Bowen Chen, Andrew Zhang, Daniel Shao, Andrew H. Song, Muhammad Shaban, Mane Williams, Anurag Vaidya, Sharifa Sahai, Lukas Oldenburg, Luca L. Weishaupt, Judy J. Wang, Walt Williams, Long Phi Le, Georg Gerber, and Faisal Mahmood. A general-purpose self-supervised model for computational pathology. *arXiv preprint arXiv:2308.15474*, 2023.
- Ting Chen, Simon Kornblith, Mohammad Norouzi, and Geoffrey Hinton. A simple framework for contrastive learning of visual representations. In *International conference on machine learning*, pages 1597–1607. PMLR, 2020.
- Xinlei Chen, Saining Xie, and Kaiming He. An empirical study of training self-supervised vision transformers. *arXiv preprint arXiv:2104.02057*, 2021.
- Ozan Ciga, Tony Xu, and Anne Louise Martel. Self supervised contrastive learning for digital histopathology. *Machine Learning with Applications*, 7:100198, 2022.
- Leonard M da Silva, Emilio M Pereira, Paulo GO Salles, Ran Godrich, Rodrigo Ceballos, Jeremy D Kunz, Adam Casson, Julian Viret, Sarat Chandarlapaty, Carlos Gil Ferreira, et al. Independent real-world application of a clinical-grade automated prostate cancer detection system. *The Journal of pathology*, 254(2):147–158, 2021.
- Olivier Dehaene, Axel Camara, Olivier Moindrot, Axel de Lavergne, and Pierre Courtiol. Self-supervision closes the gap between weak and strong supervision in histology. *arXiv preprint arXiv:2012.03583*, 2020.



- Mostafa Dehghani, Josip Djolonga, Basil Mustafa, Piotr Padlewski, Jonathan Heek, Justin Gilmer, Andreas Peter Steiner, Mathilde Caron, Robert Geirhos, Ibrahim Alabdulmohsin, et al. Scaling vision transformers to 22 billion parameters. In *International Conference on Machine Learning*, pages 7480–7512. PMLR, 2023.
- Jia Deng, Wei Dong, Richard Socher, Li-Jia Li, Kai Li, and Li Fei-Fei. Imagenet: A large-scale hierarchical image database. In *2009 IEEE conference on computer vision and pattern recognition*, pages 248–255. Ieee, 2009.
- Alexey Dosovitskiy, Lucas Beyer, Alexander Kolesnikov, Dirk Weissenborn, Xiaohua Zhai, Thomas Unterthiner, Mostafa Dehghani, Matthias Minderer, Georg Heigold, Sylvain Gelly, et al. An image is worth 16x16 words: Transformers for image recognition at scale. *arXiv preprint arXiv:2010.11929*, 2020.
- Danny Driess, Fei Xia, Mehdi SM Sajjadi, Corey Lynch, Aakanksha Chowdhery, Brian Ichter, Ayzaan Wahid, Jonathan Tompson, Quan Vuong, Tianhe Yu, et al. Palm-e: An embodied multimodal language model. *arXiv preprint arXiv:2303.03378*, 2023.
- Alexandre Filiot, Ridouane Ghermi, Antoine Olivier, Paul Jacob, Lucas Fidon, Alice Mac Kain, Charlie Saillard, and Jean-Baptiste Schiratti. Scaling self-supervised learning for histopathology with masked image modeling. *medRxiv*, pages 2023–07, 2023.
- Zoran Gatalica, Semir Vranic, Jeffrey Swensen, and Sandeep Reddy. High microsatellite instability (msi-h) colorectal carcinoma: a brief review of predictive biomarkers in the era of personalized medicine. *Familial cancer*, 15, 2016. doi:10.1007/s10689-016-9884-6.
- Simon Graham, Quoc Dang Vu, Shan E Ahmed Raza, Ayesha Azam, Yee Wah Tsang, Jin Tae Kwak, and Nasir Rajpoot. Hover-net: Simultaneous segmentation and classification of nuclei in multi-tissue histology images. *Medical image analysis*, 58:101563, 2019.
- Chuan Guo, Florian Bordes, Pascal Vincent, and Kamalika Chaudhuri. Do ssl models have d\`ej\`a vu? a case of unintended memorization in self-supervised learning. *arXiv preprint arXiv:2304.13850*, 2023.
- Samir Gupta, Dawn Provenzale, Xavier Llor, Amy L. Halverson, William Grady, Daniel C. Chung, Sigurdur Haraldsdottir, Arnold J. Markowitz, Thomas P. Slavin, Heather Hampel, Reid M. Ness, Jennifer M. Weiss, Dennis J. Ahnen, Lee-may Chen, Gregory Cooper, Dayna S. Early, Francis M. Giardiello, Micheal J. Hall, Stanley R. Hamilton, Priyanka Kanth, Jason B. Klapman, Audrey J. Lazenby, Patrick M. Lynch, Robert J. Mayer, June Mikkelsen, Shajan Peter, Scott E. Regenbogen, Mary A. Dwyer, and Ndiya Ogba. Nccn guidelines insights: Genetic/familial high-risk assessment: Colorectal, version 2.2019. *Journal of the National Comprehensive Cancer Network*, 17, 2019. doi:10.6004/jnccn.2019.0044.
- Kaiming He, Xinlei Chen, Saining Xie, Yanghao Li, Piotr Dollár, and Ross Girshick. Masked autoencoders are scalable vision learners. In *Proceedings of the IEEE/CVF conference on computer vision and pattern recognition*, pages 16000–16009, 2022.
- Dan Hendrycks and Kevin Gimpel. Gaussian error linear units (gelus). *arXiv preprint arXiv:1606.08415*, 2016.
- Gregory P. Kalemkerian, Navneet Narula, Erin B Kennedy, William A Biermann, Jessica Donington, Natasha B Leighl, Madelyn Lew, James Pantelas, Suresh S Ramalingam, Martin Reck, Anjali Saqi, Michael Simoff, Navneet Singh, and Baskaran Sundaram. Molecular testing guideline for the selection of patients with lung cancer for treatment with targeted tyrosine kinase inhibitors: American society of clinical oncology endorsement of the college of american pathologists/international association for the study of lung cancer/association for molecular pathology clinical practice guideline update. *Journal of Clinical Oncology*, 36(9), 2018. doi:10.1200/JCO.2017.76.7293.
- Mingu Kang, Heon Song, Seonwook Park, Donggeun Yoo, and Sérgio Pereira. Benchmarking self-supervised learning on diverse pathology datasets. In *Proceedings of the IEEE/CVF Conference on Computer Vision and Pattern Recognition*, pages 3344–3354, 2023.
- Jakob Nikolas Kather, Niels Halama, and Alexander Marx. 100,000 histological images of human colorectal cancer and healthy tissue. *Zenodo*, April 2018. doi:10.5281/zenodo.1214456. URL <https://doi.org/10.5281/zenodo.1214456>.
- Jakob Nikolas Kather, Johannes Krisam, Pornpimol Charoentong, Tom Luedde, Esther Herpel, Cleo-Aron Weis, Timo Gaiser, Alexander Marx, Nektarios A Valous, Dyke Ferber, et al. Predicting survival from colorectal cancer histology slides using deep learning: A retrospective multicenter study. *PLoS medicine*, 16(1):e1002730, 2019.
- Yoo Jung Kim, Hyungjoon Jang, Kyoungbun Lee, Seongkeun Park, Sung-Gyu Min, Choyeon Hong, Jeong Hwan Park, Kangeun Lee, Jisoo Kim, Wonjae Hong, et al. Paip 2019: Liver cancer segmentation challenge. *Medical image analysis*, 67:101854, 2021.
- Maxime Oquab, Timothée Darcet, Théo Moutakanni, Huy Vo, Marc Szafraniec, Vasil Khalidov, Pierre Fernandez, Daniel Haziza, Francisco Massa, Alaaeldin El-Nouby, et al. Dinov2: Learning robust visual features without supervision. *arXiv preprint arXiv:2304.07193*, 2023.



- Sudhir Perincheri, Angelique Wolf Levi, Romulo Celli, Peter Gershkovich, David Rimm, Jon Stanley Morrow, Brandon Rothrock, Patricia Raciti, David Klimstra, and John Sinard. An independent assessment of an artificial intelligence system for prostate cancer detection shows strong diagnostic accuracy. *Modern Pathology*, 34(8):1588–1595, 2021.
- Patricia Raciti, Jillian Sue, Rodrigo Ceballos, Ran Godrich, Jeremy D Kunz, Supriya Kapur, Victor Reuter, Leo Grady, Christopher Kanan, David S Klimstra, et al. Novel artificial intelligence system increases the detection of prostate cancer in whole slide images of core needle biopsies. *Modern Pathology*, 33(10):2058–2066, 2020.
- Patricia Raciti, Jillian Sue, Juan A Retamero, Rodrigo Ceballos, Ran Godrich, Jeremy D Kunz, Adam Casson, Dilip Thiagarajan, Zahra Ebrahimzadeh, Julian Viret, et al. Clinical validation of artificial intelligence-augmented pathology diagnosis demonstrates significant gains in diagnostic accuracy in prostate cancer detection. *Archives of Pathology & Laboratory Medicine*, 2022.
- David M Reese. Fundamentals–rudolf virchow and modern medicine. *Western journal of medicine*, 169(2):105, 1998.
- Myron Schultz. Rudolf virchow. *Emerging infectious diseases*, 14(9):1480, 2008.
- Shashank Shekhar, Florian Bordes, Pascal Vincent, and Ari Morcos. Objectives matter: Understanding the impact of self-supervised objectives on vision transformer representations. *arXiv preprint arXiv:2304.13089*, 2023.
- Antti Tarvainen and Harri Valpola. Mean teachers are better role models: Weight-averaged consistency targets improve semi-supervised deep learning results. *Advances in neural information processing systems*, 30, 2017.
- Bastiaan S Veeling, Jasper Linmans, Jim Winkens, Taco Cohen, and Max Welling. Rotation equivariant cnns for digital pathology. In *Medical Image Computing and Computer Assisted Intervention–MICCAI 2018: 21st International Conference, Granada, Spain, September 16-20, 2018, Proceedings, Part II 11*, pages 210–218. Springer, 2018.
- Rudolf Virchow. *Cellular Pathology as based upon physiological and pathological histology*. 1860.
- Xiyue Wang, Sen Yang, Jun Zhang, Minghui Wang, Jing Zhang, Wei Yang, Junzhou Huang, and Xiao Han. Transformer-based unsupervised contrastive learning for histopathological image classification. *Medical image analysis*, 81: 102559, 2022.
- Jason Wei, Yi Tay, Rishi Bommasani, Colin Raffel, Barret Zoph, Sebastian Borgeaud, Dani Yogatama, Maarten Bosma, Denny Zhou, Donald Metzler, et al. Emergent abilities of large language models. *arXiv preprint arXiv:2206.07682*, 2022.
- Jerry Wei, Arief Suriawinata, Bing Ren, Xiaoying Liu, Mikhail Lisovsky, Louis Vaickus, Charles Brown, Michael Baker, Naofumi Tomita, Lorenzo Torresani, et al. A petri dish for histopathology image analysis. In *Artificial Intelligence in Medicine: 19th International Conference on Artificial Intelligence in Medicine, AIME 2021, Virtual Event, June 15–18, 2021, Proceedings*, pages 11–24. Springer, 2021.
- John N Weinstein, Eric A Collisson, Gordon B Mills, Kenna R Shaw, Brad A Ozenberger, Kyle Ellrott, Ilya Shmulevich, Chris Sander, and Joshua M Stuart. The cancer genome atlas pan-cancer analysis project. *Nature genetics*, 45(10): 1113–1120, 2013.
- Zhenda Xie, Zheng Zhang, Yue Cao, Yutong Lin, Jianmin Bao, Zhuliang Yao, Qi Dai, and Han Hu. Simmim: A simple framework for masked image modeling. In *Proceedings of the IEEE/CVF Conference on Computer Vision and Pattern Recognition*, pages 9653–9663, 2022.
- Ahmet Zehir, Ryma Benayed, Ronak H Shah, Aijazuddin Syed, Sumit Middha, Hyunjae R Kim, Preethi Srinivasan, Jianjiong Gao, Debyani Chakravarty, Sean M Devlin, Matthew D Hellmann, David A Barron, Alison M Schram, Meera Hameed, Snjezana Dogan, Dara S Ross, Jaclyn F Hechtman, Deborah F DeLair, JinJuan Yao, Diana L Mandelker, Donovan T Cheng, Raghu Chandramohan, Abhinata S Mohanty, Ryan N Ptashkin, Gowtham Jayakumar, Meera Prasad, Mustafa H Syed, Anoop Balakrishnan Rema, Zhen Y Liu, Khedoudja Nafa, Laetitia Borsu, Justyna Sadowska, Jacklyn Casanova, Ruben Bacares, Iwona J Kiecka, Anna Razumova, Julie B Son, Lisa Stewart, Tessara Baldi, Kerry A Mullaney, Hikmat Al-Ahmadie, Efsevia Vakiani, Adam A Abeshouse, Alexander V Penson, Philip Jonsson, Niedzica Camacho, Matthew T Chang, Helen H Won, Benjamin E Gross, Ritika Kundra, Zachary J Heins, Hsiao-Wei Chen, Sarah Phillips, Hongxin Zhang, Jiaojiao Wang, Angelica Ochoa, Jonathan Wills, Michael Eubank, Stacy B Thomas, Stuart M Gardos, Dalicia N Reales, Jesse Galle, Robert Durany, Roy Cambria, Wassim Abida, Andrea Cercek, Darren R Feldman, Mrinal M Gounder, A Ari Hakimi, James J Harding, Gopa Iyer, Yelena Y Janjigian, Emmet J Jordan, Ciara M Kelly, Maeve A Lowery, Luc G T Morris, Antonio M Omuro, Nitya Raj, Pedram Razavi, Alexander N Shoushtari, Neerav Shukla, Tara E Soumerai, Anna M Varghese, Rona Yaeger, Jonathan Coleman, Bernard Bochner, Gregory J Riely, Leonard B Saltz, Howard I Scher, Paul J Sabbatini, Mark E Robson, David S Klimstra, Barry S Taylor, Jose Baselga, Nikolaus Schultz, David M Hyman, Maria E Arcila, David B Solit, Marc Ladanyi, and Michael F Berger. Mutational landscape of metastatic cancer revealed from prospective clinical sequencing of 10,000 patients. *Nature Medicine*, 23(6):703–713, June 2017. ISSN 1078-8956, 1546-170X. doi:10.1038/nm.4333. URL <https://www.nature.com/articles/nm.4333>.

---

Jinghao Zhou, Chen Wei, Huiyu Wang, Wei Shen, Cihang Xie, Alan Yuille, and Tao Kong. ibot: Image bert pre-training with online tokenizer. *arXiv preprint arXiv:2111.07832*, 2021.

## A Appendix

### A.1 PanMSK data

The exact tile-level data distribution is shown for the training (“train”), validation (“tune”), and testing (“test”) sets of the PanMSK dataset in Figure A1. For each tissue group, sampling of benign and cancerous tiles is balanced. All three splits follow the same data distribution across tissue groups. Virchow performance, stratified by tissue, is shown in Table A1.

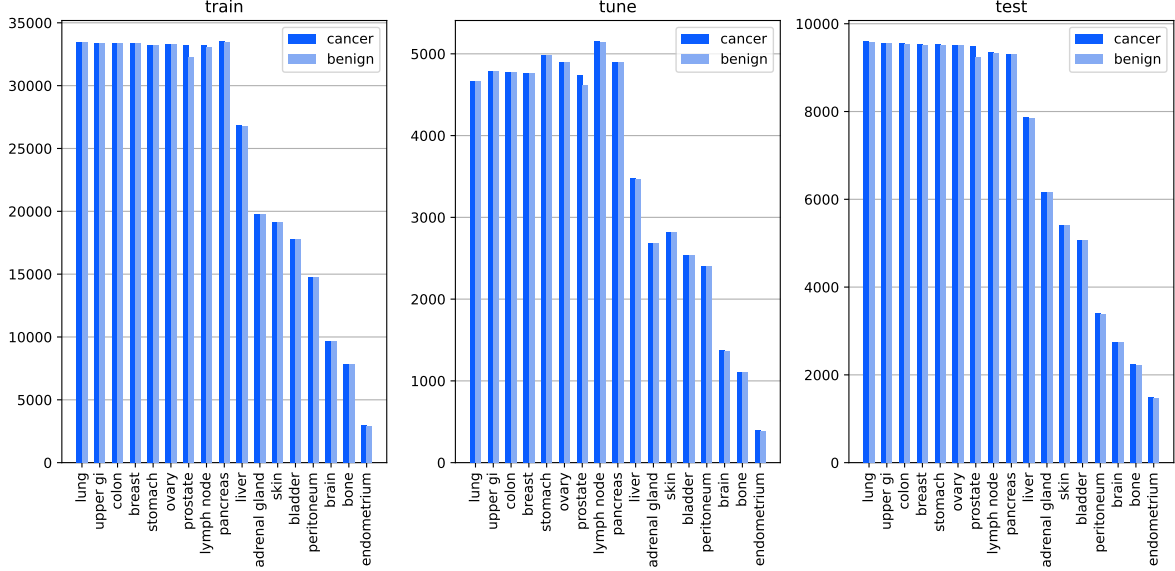


Figure A1: Distributions of cancer and benign tiles in the PanMSK dataset. The splits are balanced such that each tissue group approximately follows the same 7:1:2 (training:validation:testing) ratios in both tiles and slides counts.

Tissue	Accuracy	F1 Score
Adrenal gland	0.941	0.949
Bladder	0.981	0.986
Bone	0.957	0.973
Brain	0.928	0.927
Breast	0.880	0.885
Colon	0.922	0.922
Endometrium	0.957	0.989
Liver	0.971	0.984
Lung	0.948	0.950
Lymph node	0.928	0.935
Ovary	0.878	0.887
Pancreas	0.970	0.973
Peritoneum	0.935	0.943
Prostate	0.904	0.902
Skin	0.971	0.983
Stomach	0.824	0.883
Upper GI	0.973	0.974
Overall	0.975	0.927

Table A1: Per-tissue tile-level cancer classification performance using Virchow. Overall performance is measured by combining all tiles across all tissues prior to metric computation.

## A.2 Model details

The training process of DINOv2 as used for Virchow is shown in detail in Figure A2.

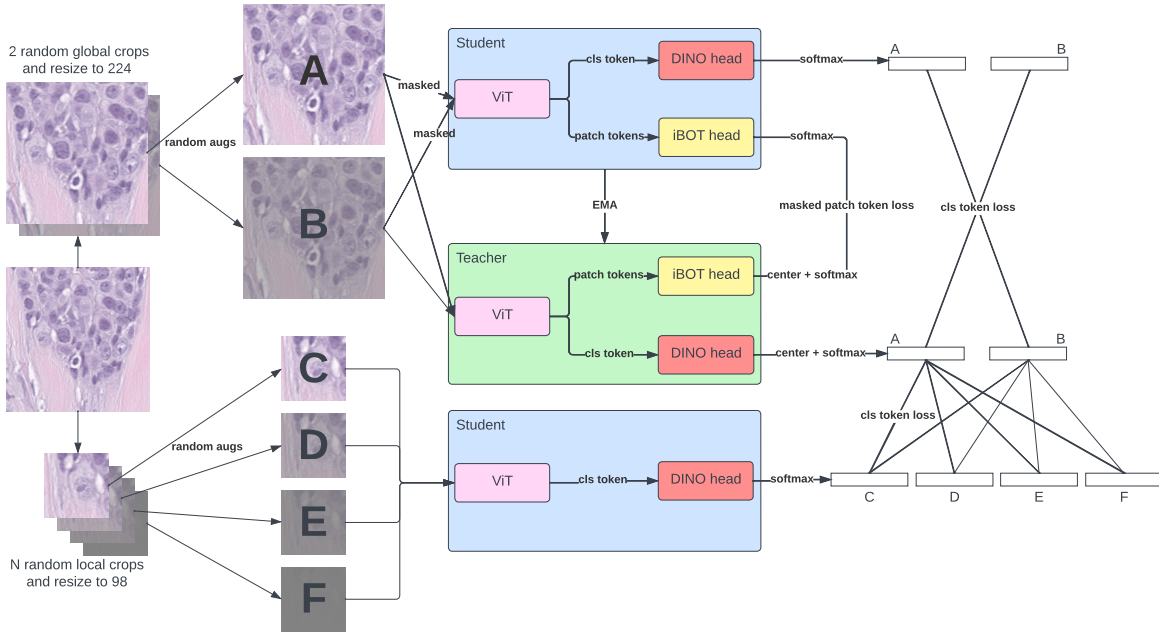


Figure A2: Schematic of DINOv2 training routine. From a single tile, 2 global crops and 8 local crops all with random augmentations are created. The global crops are randomly masked and fed to the student model while the unmasked versions are fed to the teacher model. The student tries to produce a global representation of the views (via the cls token) that matches the teacher's representation of the opposite view. The student also tries to produce representations of the masked image tokens that match the teacher's representations of the same tokens but unmasked. The local crops are only fed to the student which tries to produce a representation that matches the teacher's representations of the global crops. The teacher is an exponential moving average (EMA) copy of the student.

### A.3 Acronyms

<b>WSI</b>	whole slide image
<b>H&amp;E</b>	hematoxylin and eosin
<b>IHC</b>	immunohistochemistry
<b>TCGA</b>	The Cancer Genome Atlas
<b>HIPT</b>	Hierarchical Image Pyramid Transformer
<b>ViT</b>	vision transformer
<b>MSK</b>	Memorial Sloan Kettering
<b>iBOT</b>	image BERT pre-training with Online Tokenizer
<b>MAE</b>	masked autoencoder
<b>SGD</b>	stochastic gradient descent
<b>TNR</b>	true negative rate
<b>TPR</b>	true positive rate
<b>FPR</b>	false positive rate
<b>TP</b>	true positive
<b>TN</b>	true negative
<b>FP</b>	false positive
<b>FN</b>	false negative
<b>ID</b>	in-distribution
<b>OOD</b>	out-of-distribution
<b>mpp</b>	microns-per-pixel
<b>CRC</b>	colorectal cancer
<b>PCam</b>	PatchCamelyon
<b>MSI</b>	Microsatellite Instability
<b>FGFR</b>	Fibroblast Growth Factor Receptor
<b>EGFR</b>	Epidermal Growth Factor Receptor
<b>AUROC</b>	area under the receiver operating characteristic
<b>MSK-IMPACT</b>	MSK-Integrated Mutation Profiling of Actionable Targets
<b>dMMR</b>	deficient mismatch repair
<b>MMR</b>	mismatch repair
<b>NSCLC</b>	non-small cell lung cancer
<b>GELU</b>	Gaussian Error Linear Unit
<b>PCA</b>	principal component analysis
<b>CoNSEp</b>	colorectal nuclear segmentation and phenotypes
<b>EMA</b>	exponential moving average